Data-Clustering Analysis of Scanning Ultrafast Acoustic Experiments: Revealing Acoustic and Structural Properties of a Motoneuron

Emmanuel Péronne, Océane Sénépart, Claire Legay, Fanny Semprez, Ahmed Hamraoui, Laurent Belliard

Data-Clustering Analysis of Scanning Ultrafast Acoustic Experiments: Revealing Acoustic and Structural Properties of a Motoneuron

Emmanuel Péronne,[1,*] Océane Sénépart,[2] Claire Legay,[3] Fanny Semprez,[3] Ahmed Hamraoui,[2] and Laurent Belliard[4]

[1] *Laboratoire d'Optique Appliquée UMR7639, ENSTA-CNRS-Ecole Polytechnique IP Paris, Palaiseau, France*
[2] *Sorbonne Université, CNRS, Collège de France, Laboratoire de Chimie de la Matière Condensée de Paris, 4 Place Jussieu, Paris 75005, France*
[3] *Centre de Neurophysique, Physiologie et Pathologie, CNRS, UMR8119, Université Paris Descartes, Sorbonne Paris Cité, Paris, France*
[4] *Sorbonne Université, CNRS, Institut des Nanosciences de Paris UMR7588, 4 Place Jussieu, Paris 75005, France*

(Received 13 December 2021; revised 31 May 2022; accepted 13 July 2022; published 20 September 2022)

Ultrafast acoustic imaging experiments are a powerful tool to investigate, at the nanometer scale, cell mechanical properties such as stiffness, viscosity, and adhesion, properties that play some roles in the life and death of cells. However, due to cell complex structures, the ultrafast acoustic signal analysis is quite intricate and depends on multiple parameters. Complex data analysis with poorly known parameters can be handled by a data clustering method as already shown in particle physics and biology. In this work, ultrafast acoustic data analysis is tackled by a spectral clustering method followed by a hierarchical agglomerating method. Coupled to conventional microscopy performed on the very same cell, the clustered data can be assigned to inner-cell features such as the nucleus, the cytoplasm, and the cytoskeleton. The signal dependency on the cell thickness and stiffness is highlighted. Moreover, thanks to the improvement of the signal-to-noise ratio, the nature of the adhesion is also assessed through observation and characterization of a polymerlike layer as thin as a few nanometers.

DOI: 10.1103/PhysRevApplied.18.034051

I. INTRODUCTION

It is known that the external forces exerted on cells can have a strong influence on physiological processes through the mechanotransduction processes [1]. They may drive the cell differentiation into osteocytes or neurons, for example. Among all the techniques, which can be used to probe the cell mechanical properties [2], this work is based on a scanning ultrafast acoustic microscope (SUAM) to investigate cell stiffness, viscosity, and adhesion. SUAM is a pump-probe technique that samples the acoustic response in time (t) at different locations (x, y). It can be performed in transmission where the cell optical properties are measured while a short acoustic pulse is propagating through the cell. Transmission signal is typically composed of oscillations resulting from the interaction between the light and the acoustic pulse propagating into the cell and usually called Brillouin oscillations (BOs). Scanning the BO properties (amplitude, frequency, lifetime, and phase) allows bulk elasticity in biological cells to be mapped [3]. In-plane or in-depth investigations [4–8] can reveal nucleus or cytoskeleton elasticity and thickness of the cell. This optical technique is very convenient for designing a specific environment to study living cells [9,10].

SUAM can also be performed in reflection where an acoustic echo is bouncing back and forth on the transducer-cell interface. The echo's temporal shape can reveal the spatial and dynamical properties of the cell adhesion [11–13]. Ultimately, as previously shown [14,15], both measurements can be combined to get correlated information on the cell mechanical properties. SUAM experiments are facing two challenges: improving the SNR and easing the data analysis. The total data acquisition time is given by $N\delta$ where N is the number of data sampling points and δ is the acquisition time of a single data point. A trade-off has then to be found between the SNR (which is proportional to $\delta^{-1/2}$) and spatiotemporal resolution in order to catch the cell's inner features while keeping the total data acquisition time manageable. Moreover, due to the inhomogeneity of the cell, the transient acoustic signal is highly dependent on the investigated spot. Mapping cell mechanical properties may then require cumbersome spot-by-spot analysis with multiparameter fit functions. We have shown in a previous work that it is possible to alleviate the constraints of the mapping by sorting the different spots according to the likeness (i.e., the similarity) of the temporal shape

*emmanuel.peronne@ensta-paris.fr

of the signal [7]. For example, the nucleus can be spatially resolved and its corresponding averaged signal can be computed, simplifying the subsequent data analysis. Such a procedure requires some prior knowledge of the cell structure in order to find the sample spots with good similarity with all the nucleus spots.

Data clustering (or cluster analysis) aims at sorting a large dataset into smaller datasets (i.e., clusters) such that data within a given cluster are more similar to each other than to those in other clusters. Data clustering is a powerful tool used in almost every aspect of science and is at the core of deep learning techniques. In physics, data clustering is vastly used in particle physics and cosmology for event detection as small as Higgs boson or as large as gravitational waves. In biology, data clustering is also widely applied to achieve sequencing as well as diagnostics. Since there are many data-clustering methods, the clustering algorithm (with its similarity criteria) has to be chosen carefully depending on the dataset properties and the expected clusters. In this paper we propose to make use of data-clustering techniques in order to sort the experimental data in order to map the cell properties without prior knowledge of the cell structure. Indeed, using a single fit function to map the whole cell acoustic properties requires several fitting parameters. Such a fit function must arise from a complex model of the intrinsic cell inhomogeneity based on prior knowledge. Therefore, small structures or unexpected ones can be missed during the analysis.

In the following, after a short description of the sample and the SUAM apparatus, the choice of the clustering method is detailed. The proposed clustering method occurs in two successive steps: a spectral clustering method [16] followed by a hierarchical agglomerative method. The results are then discussed and compared to other imaging techniques, providing a fast identification of the different cluster features. In particular, the clustered acoustic map is analyzed in the light of atomic force and fluorescence microscope images, strengthening the consistency of the data-clustering analysis in SUAM experiments.

II. SAMPLE PREPARATION, EXPERIMENTAL SET UP, AND DATA PROCESSING

A. Cell culture and fixation

The motoneurons used in this study are immortalized mouse motoneurons called MN1. They are cultured on a biocompatible titanium layer sputtered on sapphire substrate 3 days before fixation. A grid of numbers has been laid out in gold by lithography and chemical etching on top of the titanium layer (300 nm thick) for labeling purpose. Thanks to the grid, each cell can be labeled and then studied with different techniques. Fixation is performed with glutaraldehyde [2% in phosphate-buffered saline (PBS)] at room temperature during 15–20 min. Cells are washed twice with PBS for 5 min, quickly rinsed with deionized water to remove salts and then dried under a moderate stream of nitrogen. The motoneurons studied are fixed, which means the cells are not active anymore but retained most of their morphological characteristics. This protocol makes it possible to carry out studies in the open air without degradation or motion of the cell during the SUAM acquisition. The effect of cell fixation on the mechanical properties of the cell is not perfectly known, but the cell is supposed to keep the same differential in mechanical properties between fixed condition and *in vitro*.

B. Conventional cell imaging

With the help of the gold lithographed labels, the same cells can be characterized with different set ups. The optical images of MN1 cells cultured on the Ti layer are realized in an episcopic geometry with white light and 20× bright-field objectives. As can be seen in Fig. 1(a), the cell (as well as part of the gold labels) is mapped but inner structures of the cell are hidden by the interference effect due to cell transparency.

In order to identify the nucleus within the cell body, MN1 cells are labeled using immunohistochemistry [17]. Cells are incubated overnight at 4 °C with a rabbit polyclonal anti-β actin (1 μg ml^{-1}); three 10-min washes are carried out with PBS tween 0.1%. Cells are then incubated 1 h at room temperature with a secondary antibody coupled to Alexa Fluor 488 goat antirabbit at dilution 1/500 (Thermo Fisher Scientific: 10729174). Nuclei are labeled with DAPI. Thanks to the fluorescent markers, the cell body and the nucleus are readily localized altogether by fluorescent imaging as shown in Figs. 1(b) and 1(c).

Moreover, the cell topography is characterized with the help of an atomic force microscope. MN1 cells cultured on the Ti layer are imaged using a Digital Instruments AFM (Veeco). Contact mode is operated with Veeco RTESP tip cantilevers spring constant: 4 N m^{-1} and 256 lines 512 pixels images are acquired at a scanning frequency of 1 Hz. The system includes an integrated optical microscope, allowing prepositioning of the AFM tip over the cells. The topography of the cell labeled 658 is shown in Fig. 1(d), illustrating how the fixed cell thickness is quite constant at the nucleus location and decreases away from the nucleus.

C. Scanning ultrafast acoustic experiment

A Ti:sapphire femtosecond laser beam operating at 800 nm and 80 MHz (MaiTai®) is split into two beams. The pump beam is focused down to 2 μm on the Ti layer through the sapphire substrate and is modulated at 1.8 MHz. Since the pump beam is absorbed within the first few tens of nanometers of the Ti layer in approximately 100 fs, it induces a sudden thermal expansion, which will give rise to a transient acoustic pulse about 6 ps long. The acoustic pulse is then propagating through the Ti layer

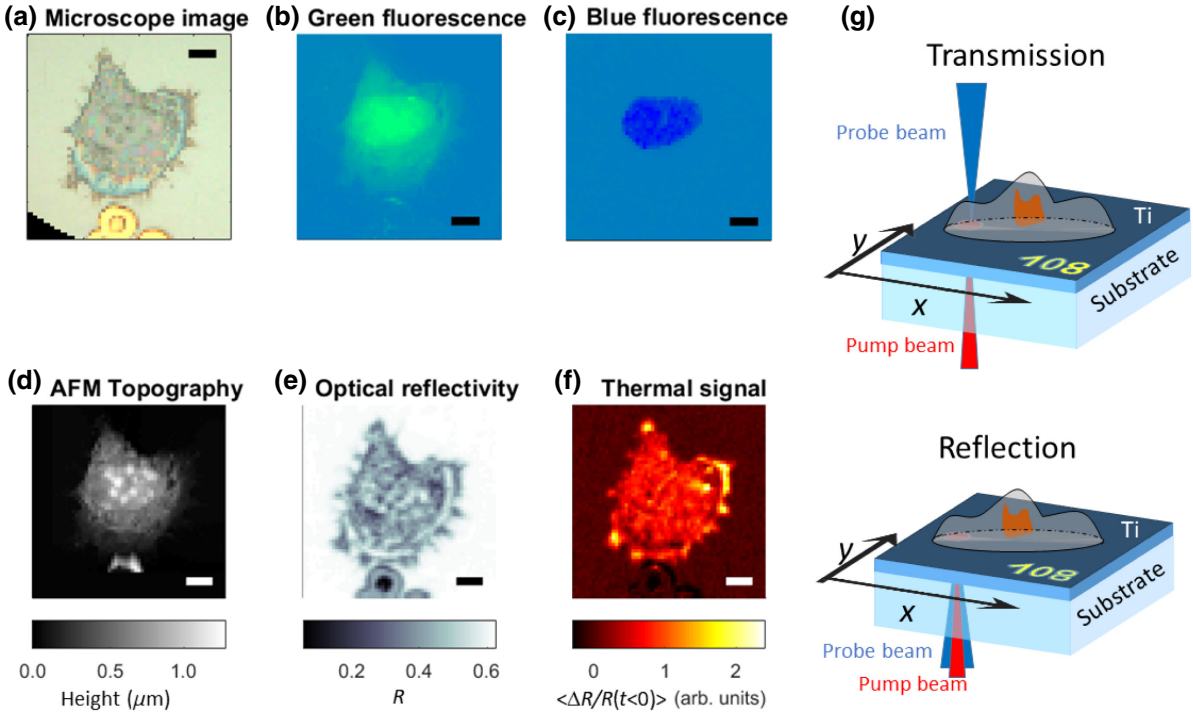

FIG. 1. Motoneuron cell imaged with four different techniques. Inserted scale bars are 10 μm wide for all maps. (a) Bright-field image of the motoneuron cell close to gold label 658 (partially visible). (b),(c) Fluorescence images of the same cell as (a). The green fluorescence points out the cytoskeleton rich in actin. The blue fluorescence image highlights the nucleus material (d) Cell topography measured by an atomic force microscope in contact mode. (e) Cell optical reflectivity measured at 400 nm as measured by SUAM experiments. (f) Thermal response due to the accumulated heat induced by the pump modulated at 1.8 MHz during SUAM experiments. Spatial resolution of maps (a)–(d) have been numerically lowered to match the SUAM maps' resolution. (g) Sketch of the scanning ultrafast acoustic microscope to map mechanical cell properties in transmission (top) or reflection (bottom) configuration. Sample position is controlled along the x and y axis while the pump beam (red) is incident on the Ti layer and the probe beam (blue) is focused through the cell (top) or through the substrate (bottom).

and is partially reflected at the Ti layer and cell interface or totally reflected if there is no cell. The acoustic pulse, which is propagating in the cell may bounce back at the cell surface. The probe beam is frequency doubled through a BBO crystal and is focused down to 2 μm and overlapped with the pump spot. The probe beam is either copropagating with the pump (referred to as reflection set up) or counterpropagating (referred to as the transmission set up), as illustrated in Fig. 1(g) and is used to measure the sample reflectivity R. The pump-induced change of reflectivity $[\Delta R(t = t_{\text{probe}} - t_{\text{pump}}, x, y)]$ of the sample is then measured with the help of a lock-in amplifier either in the reflection (the sapphire substrate side) or the transmission configuration (the cell side), respectively. In reflection configuration, the probe is also absorbed within the few tens of nanometers therefore the probe is mainly sensitive to the acoustic pulse, which is totally or partially reflected at the titanium surface. Reflected acoustic pulses are commonly mentioned as acoustic echos. In transmission configuration, the probe is weakly absorbed through the cell and is reflected by the Ti layer as well. In this case, the probe is diffracted by the acoustic pulse propagating through the cell leading to the so-called Brillouin oscillation. The delay $t = t_{\text{probe}} - t_{\text{pump}}$ is controlled with a translation stage and the sample is mounted on a two-axis (x, y) translation stage to spatially resolve ΔR. Two sets of 60 μm $\times$ 60 μm experimental data are recorded for cell 658 in transmission and reflection geometry every 4 ps or 1 ps, respectively (i.e., time resolution of $t = t_{\text{probe}} - t_{\text{pump}}$).

Figure 1(e) shows the reflectivity R measured by the SUAM set up with a 400-nm probe and Fig. 1(f) displays a photothermal map of the cell $\langle \Delta R/R \rangle_{(t<0)}(x, y)$ obtained by averaging the relative change of reflectivity just before the pump excitation. Like the bright-field image, the cell is precisely localized by optical reflectivity in the transmission scheme but the inner-cell features are not resolved due to several factors affecting the cell reflectivity (surface roughness, orientation, surface impurities, etc.). The thermal mapping is possible because the absorption of the pump pulses induce a steady heating of the sample, which modifies locally the optical index. According to the thermal map, the photothermal signal is larger at the edge of the cell where the probe is less reflected. This may be explained by heat accumulation in the thinner part of

the cell due to reduced diffusivity and increased optical absorption (enhancing the sensitivity to changes of optical index).

D. Data processing

It is known that the acoustic signal, measured in transmission geometry, can be used to catch the inner-cell structures [4–14]. As illustrated in our previous work [7,15] the nucleus can be resolved, for example, by sorting the cell signal according to the cross-correlation map. Such maps are obtained by computing for all the measured spots the Pearson correlation coefficient with the pump-probe signal measured at a well-chosen spot (the reference signal). When looking at the correlation map obtained for a reference signal chosen in the gold label, the cell, the bare transducer and the gold label can be mapped right away, as shown by the cross-correlation map in Fig. 2(a). Indeed, computing the cross-correlation of the pump-probe signal allows evaluation of the acoustic likeness of all the points with the reference point. By inspecting the distribution of the cross-correlation coefficient displayed in Fig. 2(b), three clusters can be identified and attributed to the cell, the bare Ti, and the gold label as illustrated in Fig. 2(c).

The pump-probe signal averaged within each cluster is shown in Fig. 2(d). At 0 ps the acoustic pulse arrival at the Ti surface is clearly visible when probing the Ti layer only (bottom curve). When probing through the cell (top curve), the acoustic pulse signature is hidden by the onset of the Brillouin oscillation, which is visible up to 100 ps.

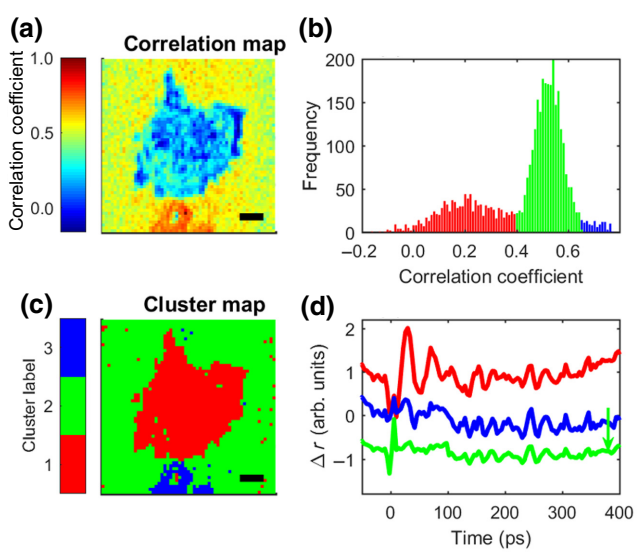

FIG. 2. Acoustic mapping of the cell with correlation technique (see Ref. [7]). Inserted scale bars are 10 μm wide. (a) Correlation map obtained for a spot chosen on the gold label. (b) Corresponding correlation coefficients colored according to their value. (c) Acoustic map given by the three correlation coefficient distributions. (d) Corresponding acoustic signal depending on pump-probe delay $t_{\text{probe}} - t_{\text{pump}}$ and averaged within each cluster.

After 200 ps all three signals display the same features, which are related to slow laser-power drifting during the acquisition and may overshadow signal related to cell features. Only the acoustic signal associated to the cell (top curve) presents Brillouin oscillations and provides information on the elastic properties of the cell through its period, which is proportional to cell sound velocity and through its damping, which is related to the cell viscosity.

Since this work is focusing on resolving inner-cell acoustic features, the mean acoustic response $\langle \Delta R/R \rangle_{(x,y)\in\text{Ti}}(t)$ arising from the Ti transducer alone [see Fig. 2(d) green curve] is subtracted to the whole set of $\Delta R/R(x,y,t)$. It is then possible to chose an alternative reference signal within the cell in order to identify some clusters of Pearson correlation coefficients within the cell and to get a more detailed map. However, the reference signal cannot be chosen randomly as many reference signals produce a noisy map. Is it, then, possible to compute the best reference signal? In fact, is a reference signal even required? Answers are yes and no, respectively. Indeed all the correlation maps, obtained when each spot is chosen to provide the reference signal, bare their own information. Thanks to data-cluster analysis, it is possible to make use of all the correlation maps to sort all the pump-probe signal according to their correlation likeness. From now on, the three-dimensional (3D) $N_x \times N_y \times N_t$ SUAM data, free of the Ti transducer response, are reorganized as a two-dimensional (2D) data set, which can be understood as a collection of $N = N_x \times N_y$ independent observations (measured at a different spot), each observation being characterized by its N_t measurements (i.e., the pump-probe signal).

III. DATA CLUSTERING

In the following, the N observations (or pump-probe signals), which have been recorded at different spots are clustered according to their temporal variation (i.e., the N_t measurements) by applying a spectral clustering method [16]. Spectral clustering methods have been chosen because they are known to produce high-quality clustering on small data sets (at a cost of its computational complexity, which is not well suited for the large-scale problem). It requires a choice of pairwise distance in order to evaluate how close observations are between each other. Following our previous work [7,15], the pairwise distance of this work is based on the Pearson correlation coefficient. It requires also the number of clusters k to look for to be fixed, which is unknown at first but which can be handled in a smart way thanks to a hierarchical agglomerative clustering. The main idea is to start with a large number of clusters obtained by the spectral clustering method and reduce this number by merging the two closest clusters hierarchically. The hierarchy of the merged cluster maps obtained with this method is shown in Fig. 3 and is discussed in the following.

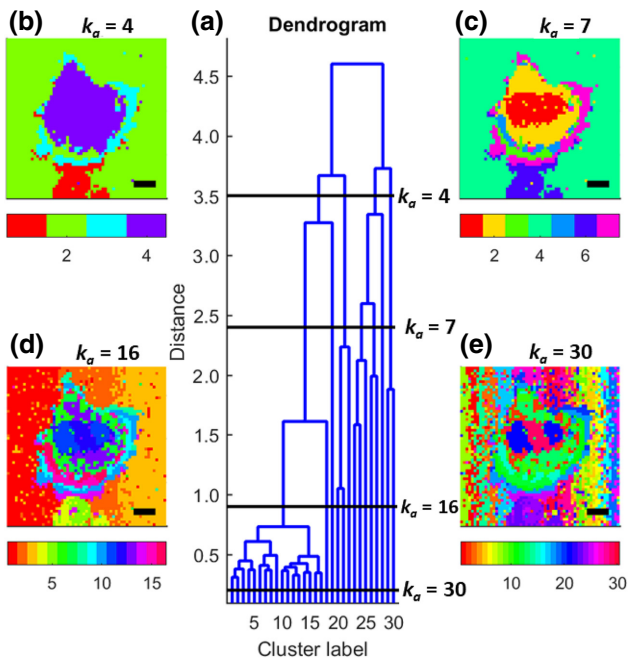

FIG. 3. (a) Dendrogram corresponding to the agglomerative hierarchical clustering of 30 clusters obtained by spectral clustering. The agglomerated cluster map corresponding to the cuts at $k_a = 4$, 7, 16, and 30 clusters in the dendrogram are displayed around and labeled, respectively, (b)–(e). Map (e) displays the clustering as obtained from the spectral clustering method. The colorbars provide the correspondences between the cluster colors used in the maps and the cluster labels used in the text and all the inserted scale bars are 10 μm wide.

A. Spectral clustering method

The first step of the clustering is based on the approach of Meilä *et al.* (Ref. [18]) categorized as a spectral clustering method. In brief, this method is looking for the first largest k eigenvalues and eigenvectors of a graph Laplacian matrix $L = D - S$, where S is the similarity matrix and $D = \sum_i S_{ij}\,\delta_{ij}$ $(0 \le S_{ij} \le 1, 1 \le i \le N, 1 \le j \le N)$. The L_{ij} coefficients can then be interpreted as the probability to "jump" from i to j in a random walk process. The k clusters are then found by applying a k-means algorithm to the set of k-calculated eigenvectors. This spectral clustering requires only a choice of similarity function and the number of clusters k. A similarity coefficient $S_{ij} = 1$ means perfect matching between i and j while $S_{ij} = 0$ means i and j are totally different. Among all the possibilities to calculate a similarity matrix, this work uses the one based on the Pearson correlation between the pump-probe signals recorded at spots i and j such that $S_{ij} = 0.5 \times (\mathrm{xcorr}(i,j) + 1)$. Since the pertinent number of clusters is not known, k must be chosen as large as possible while keeping the number of observations clustered together large enough to provide a meaningful averaged observation. That is why we propose to set it as the ratio between the total number of pixels over the number of pixels of the smallest feature, which is expected to be clustered. For example, in order to find a cluster associated with the gold label partially scanned by the SUAM experiment, the number of clusters can be chosen around $k = 30$.

The result of the spectral clustering method [19], shown in Fig. 3(e), does provide some inner-cell structures. However, it fails to catch the bare part of the sample (titanium only) as a single cluster and provides more than ten clusters instead. Indeed, the spectral clustering method tends to produce clusters of roughly equal size when all the data share some similarities with all the others (i.e., clustering a fully connected graph). It appears that the spectral method has clustered the data also according to noisy features or experimental biases. However, a quick inspection of the averaged signal associated to each cluster shows that some of those clusters should be merged into a single larger cluster.

B. Hierarchical agglomerating clustering method

The main idea of this second clustering step is to merge clusters with similar averaged signals. This merging can be achieved with a hierarchical agglomerating clustering method, which compares all the mean signals pairwise and finds the two closest ones to merge them and, then, which repeats this process using a mean signal for the newly merged clusters. Since each iteration merges two clusters, this process is repeated until all the clusters are merged in a single cluster. To visualize how and when the clusters are merged one can produce a dendrogram, as shown in Fig. 3(a). With the help of the dendrogram, it is possible to choose the number of relevant clusters by looking at the cluster map obtained at a given depth k_a of the dendrogram. At $k_a = 16$ clusters depth [see Fig. 3(d)], most of the spectral clusters associate with bare Ti signal are merged into three agglomerated clusters. At the depth of $k_a = 7$ clusters [Fig. 3(c)], the bare Ti layer and the gold label appear as single clusters and some cell inner structures are clearly identified such as the nucleus (agglomerated cluster number 1) as well as the cell thin periphery (agglomerated cluster number 7). At the depth of $k_a = 4$ agglomerated clusters [Fig. 3(a)], most of the cell features disappear providing acoustic map comparable to what is obtained from cross-correlation maps [Fig. 3(b)]. This figure illustrates how the final choice of the number of agglomerated clusters k_a can be set with a very small amount of knowledge of the sample.

IV. ANALYSIS AND DISCUSSION

A. Brillouin oscillation analysis as measured in transmission

Let us fix the numbers of agglomerated clusters k_a such that (1) the bare Ti area appears as a single cluster; (2) the

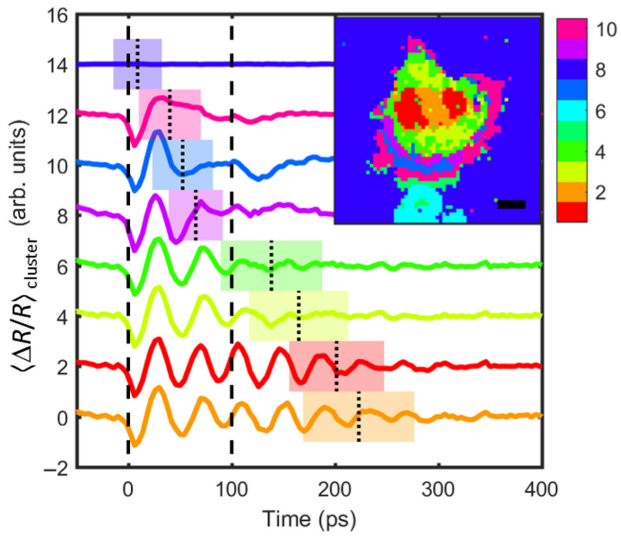

FIG. 4. Acoustic signals averaged within each cluster associated to cell structures when $k_a = 10$. The dashed vertical line marks the arrival time of the pulse echo having done an additional round trip within the metallic transducer. The small vertical dotted lines mark the estimated arrival time of the acoustic pulse at the cell surface according to the AFM topography. The surrounded shaded areas stand for the plus or minus root-mean-square uncertainty when averaging the cell height. Inset: $k_a = 10$ clusters map with a 10-μm-wide scale bar. Averaged signals from noncell clusters 5 and 6 are not shown (see text).

number of cell clusters is minimum; (3) the nucleus is still given by two distinct clusters. These conditions lead to a number of $k_a = 10$ agglomerated clusters and the resulting cluster map is shown in Fig. 4 (inset). At the depth of $k_a = 9$ clusters, the two nucleus clusters merged while at $k_a = 11$ an inner cell cluster splits into two spatially entangled clusters. At first glance, the cluster map shows a good qualitative agreement with the fluorescence map and the AFM map. However, it is useful to check if the clusters can be associated to specific properties of the cell and if the noise or the experimental biases have influenced in some way the clustering.

The ten clusters can be compared between them according to their different physical properties, which are gathered in Table I. Thanks to the fluorescence, each pixel can be assigned to the nucleus (blue fluorescence), the cell (green fluorescence), or the bare titanium (no fluorescence) such that each fluorescent component can be weighted for the clusters as shown in Table I. Clusters 1 and 2 nicely match the blue fluorescent area (> 92%) while clusters 6 and 8 match the nonfluorescent area up to 97% making their respective assignment pretty straightforward. Assignment of clusters 3, 4, 7, 8, and 9 to "cytoplasm" and "edge" is possible thanks to the averaged heights and averaged SUAM photothermal signal gathered in Table I as well (see Fig. 1 for the corresponding maps). Averaged optical reflectivity is also computed to confirm its weak influence on the clustering results (except for clustering the bare Ti area). Cluster 5 is labeled as outliers since it is mainly nonfluorescent while associated to a 240-nm-thick cell and, therefore, cannot be assigned strictly to the cell or the bare Ti.

The labeling of the clusters is further enforced by analyzing the acoustic signal averaged within each agglomerated clusters. The result is plotted in Fig. 4 where the line colors match the cluster colors of the inset map. A slow varying background (second-order polynomial) is subtracted to emphasize the Brillouin oscillations, typical of acoustic cell signal. Signals are vertically shifted for better clarity. The signals found by the clustering are consistent with what were found previously with the cross-correlation clustering [7,15]. The nucleus (clusters 1 and 2) is associated to higher BO frequencies and longer BO lifetime compared to dried cytoplasm (clusters 3, 4, and 9), which are associated to lower frequencies and shorter lifetime. The cell edge (clusters 7 and 10) is characterized by a partial BO. Clusters 6 (averaged signal not shown) and 8 correspond to the gold label and the bare Ti, respectively. Cluster 5, not shown, is associated to a low-amplitude

TABLE I. Cluster properties deduced from comparisons with fluorescent images (in %) and by averaging the height measured by AFM (in nm), the optical reflectivity R or the photothermal signal $\langle \Delta R/R \rangle_{t<0}$ measured by the SUAM (both in arb. units). Cluster sizes are given in number of pixels. Each cluster is labeled accordingly: nucleus, cytoplasm, edge of the cell (edge), gold label (gold), bare titanium (titanium) or outliers.

Cluster Nb	1	2	3	4	5	6	7	8	9	10
Size	121	103	151	229	73	133	89	2385	70	246
Blue fluo. (%)	99	92	27	22	0	0	0	0	1	0
Green fluo. (%)	1	8	72	76	16	2	94	3	97	48
No fluo. (%)	0	0	1	2	84	98	6	97	1	52
Height (nm)	746	825	561	471	241	282	194	33	241	149
Thermal signal	0.74	0.78	0.7	0.64	0.00	−0.21	0.31	0.01	0.53	0.90
Reflectivity	0.44	0.42	0.41	0.39	0.42	0.39	0.43	0.61	0.42	0.47
Assignment	Nucleus	Nucleus	Cytoplasm	Cytoplasm	outliers	Gold	Edge	Titanium	Cytoplasm	Edge

signal such that the clustering seems more based on noise structure rather than signal.

The vertical dashed lines mark the arrival time of the acoustic pulse and its echo generated within the transducer. Both acoustic pulses generate signals, which are overlapping in time. Both signals can be in phase leading to an increase of BO amplitude (as for the nucleus signal) or out of phase leading to a decrease of the BO amplitude (as for the cytoplasm). The reflection at the cell surface is also known to produce a phase change in the BO, which can be used to monitor the cell thickness. Thanks to the AFM cell map and the labeling of the clusters done in Table I, the averaged signals are well understood. It is also known that the BO frequency is expected to be different between the nucleus and the cytoplasm. Accordingly, the cytoplasm clusters 3 and 4 exhibit low BO frequencies around 23 GHz, whereas the nucleus clusters 1 and 2 exhibits a frequency around 25.5 and 24.5 GHz, respectively. BO frequencies of clusters 7, 9, and 10 are harder to measure precisely since the phase change due to the reflection occurs before a full BO period, but the value is getting back around 25 GHz. A better fit of the BO frequency would require an analytical model like in Ref. [20] which takes into account all the reflections (acoustical and optical) in a bilayer system on semi-infinite substrate (Ti + cell on sapphire).

Given a sound velocity of 3.4 μm ns^{-1} for the cytoplasm clusters and 3.7 μm ns^{-1} for the other clusters, deduced from the Brillouin frequencies, the acoustic reflection at the cell surface is computed and indicated by the individual short vertical dotted lines. It is quite remarkable how the changes in amplitude or phase in the BO matched the estimated arrival time of the acoustic echo at the cell surface demonstrating how thickness dependent the clustering result is. Assuming that the edge signal is dominated by the cytoskeleton of the cell, one can argue that the nucleus and the cytoskeleton have comparable acoustic properties while the thick cytoplasmic part of the cell (clusters 3 and 4) is less dense or less rigid. Moreover, the differences between clusters 1 and 2 (see Table I and Fig. 4), which imply different acoustic properties, suggest that the cell has been fixed while starting mitosis.

B. Echo analysis as measured in reflection

In ultrafast acoustic experiments performed in a reflection configuration, the acoustic echo, which reflects at the transducer-cell interface is investigated [21]. Such a configuration is quite attractive since the cell is not perturbed by the laser, making this kind of experiment suitable for studying living cell. However, investigating cells *in vitro* is quite challenging because of the nutritive environment, which is surrounding the cells. Indeed, it decreases the acoustic impedance mismatch between the cells and its environment. Here, the clustering data treatment is applied

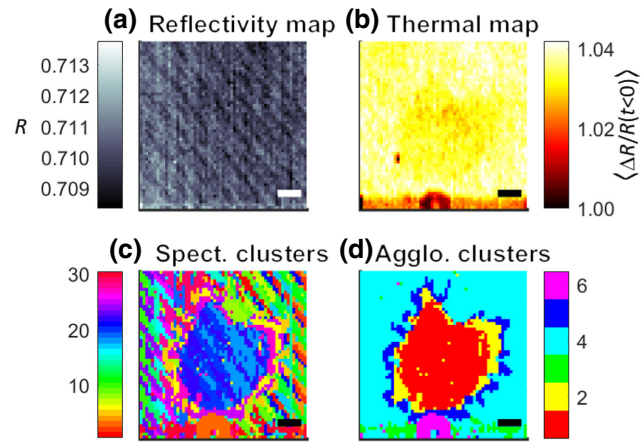

FIG. 5. Cell mapping in the reflectivity configuration (pump and probe incident on the transducer on the opposite side of the cell). Inserted scale bars are 10 μm wide for all maps. (a) Optical reflectivity map. (b) Thermal map. (c) Acoustic mapping with spectral clustering. (d) Acoustic map after cluster agglomeration down to six clusters.

to the reflection configuration in order to test the signal-to-noise ratio in such an imaging technique. The optical reflectivity in reflection configuration, shown in Fig. 5(a), is featureless as expected. However, by integrating the signal 40 ps prior to the echo arrival (i.e., during the thermal decay of the transducer after pump excitation), the cell can be spotted as illustrated on the thermal map in Fig. 5(b). The observation originates from the modification of the thermal boundary at the transducer-free surface wherever there is a cell or not. While weak, the thermal signature is still measurable in reflection configuration. Note that the thermal image of the cell looks saturated due to the strong thermal response of the gold label. As in the transmission configuration, the bare Ti signal is obtained from cross-correlation imaging and then subtracted to the data set before spectral clustering. As demonstrated by the 30-cluster result, as plotted in Fig. 5(c), the acoustic signature of the cell is caught by the spectral clustering as well as in transmission. The agglomerative clustering down to six clusters, shown in Fig. 5(d), provides a clear picture of the cell with a core cell cluster (cluster 1) surrounded by two concentric peripheral clusters (clusters 2 and 5). The gold label and the bare Ti layer are retrieved as well (clusters 6 and 4, respectively). Cluster 3 arises from some experimental artifact as indicated by the bottom of the raw optical reflectivity and the thermal maps. It illustrates how data clustering can help to handle noisy data.

In order to investigate the origin of the clusters, the acoustic signal is averaged within each cluster and is then compared to the reference acoustic signal, which is the signal measured within the bare Ti cluster. The differences between the cell signals (clusters 1, 2, and 5) and the reference signal (cluster 4) are shown in Fig. 6 along with

the reference signal (black dotted curve, rescaled and vertically shifted). Up to 10 ps, the acoustic signals for clusters 1 and 2 are quite similar while the cluster 5 is half in amplitude. At longer pump-probe delay, signals from clusters 2 and 5 converge to 0, i.e., there is no difference between the acoustic signal of clusters 2 and 5 and the reference signal. However, the difference between cluster 1 signal and the reference signal remains constant at longer delay. It is shown in the following that those observations are consistent with the presence of a very thin and soft adhesion layer between the transducer and the cell.

When the acoustic pulse reflects at the transducer surface, the thin layer starts to "ring," producing the trailing oscillation in the signal in Fig. 6. The experimental determination of the acoustic properties of the thin layer are resumed in Table I. The traveling time is given by the ringing period. The acoustic impedance mismatch is found by inspecting the amplitude of the ratio of the Fourier transforms of the cluster signals at low frequency (below 100 GHz). As can be seen from Table II, the difference in amplitude of the signal between cluster 5 and clusters 1–2 is an indication of different acoustic impedance. Since the impedance mismatch may be due to a change of the sound velocity, the mass density or both, the signals are analyzed depending on two different assumptions (see Table II): (b) layer density is assumed and (c) sound velocity is assumed. Depending on the assumption, the thin layer sound velocity is more likely to vary between 1.28 nm ps^{-1} and 2.5 nm ps^{-1} (i.e., a layer thickness between 4.53 and 8.88 nm) and the mass density between 0.66 g cm^{-3} and 1.3 g cm^{-3}, which are typical values for organic polymers.

Another striking feature in Fig. 6 is the difference of signal between cluster 1 and the others at longer time. It implies that the acoustic transmission between the thin layer and the cell is greater for cluster 1 than for the others.

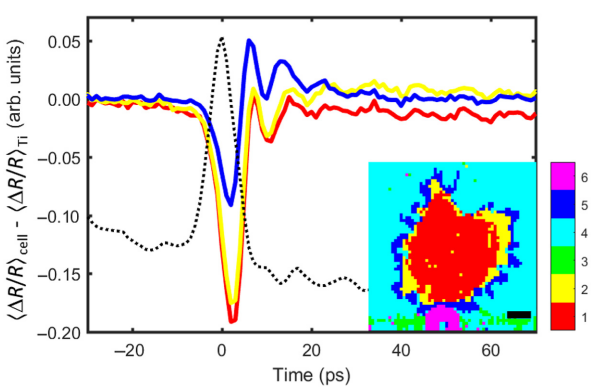

FIG. 6. Cell acoustic differential reflectivity averaged for each cell cluster. The cell clusters, numbered 1, 2, and 5, are shown on the inset map (the scale bar is 10 μm wide). The dotted black curve shows the bare Ti reflectivity ($\times\frac{1}{4}$) obtained after averaging the signal of cluster 3 and used as the reference signal to measure the differential acoustic reflectivity.

TABLE II. Adhesion layer properties depending on the cluster. (a) The impedance layer is calculated with $Z_{\mathrm{Ti}} = 27.38$ MRayls. (b) The density $\rho_l = 1.3$ g cm^{-3} is assumed. (c) The sound velocity $c = 2.5$ nm ps^{-1} is assumed.

	Cluster 1	Cluster 2	Cluster 5
Ringing period (ps)	7.1	7.1	7.1
R_{acoustic}	0.83	0.84	0.89
$Z_{\mathrm{layer}}/Z_{\mathrm{Ti}}$ (10^{-2})	9.1	8.6	6.1
Z_{layer} (MRayls) (a)	2.5	2.36	1.66
Thickness 1 (nm) (b)	6.83	6.45	4.53
Velocity 1 (nm ps^{-1}) (b)	1.92	1.81	1.28
Thickness 2 (nm) (c)	8.88	8.88	8.88
Density 2 (g cm^{-3}) (c)	1.00	0.95	0.66
Cluster projection on the following:			
Nucleus	0.27	0.02	0
Cytoplasm	0.51	0.07	0.01
Edge	0.19	0.57	0.07
Ti	0.03	0.35	0.91

In contrast, clusters 2 and 5 do not seem to be associated with the transmission in the cell. This is confirmed by the decomposition of the clusters on the clusters measured in transmission as shown in Table II, 97% of the point in cluster 1 corresponds to nucleus or cytoplasm clusters, while 91% of cluster 5 corresponds to the Ti cluster. Cluster 2 corresponds to an intermediate case with 56% of edge clusters and 31% of the Ti cluster.

V. CONCLUSIONS

The acoustic properties of fixed motoneurons have been investigated with the help of a scanning ultrafast acoustic microscopic apparatus where the sample can be probed on the cell side or on the transducer side, and which allow both measurements to be correlated. Thanks to a clustering method of the data, which require less prior knowledge of the cell structure, the inner-cell acoustic features are enlightened. After a first clustering with a correlation method to get the signal coming from the Ti substrate, the cell data are then clustered by a spectral clustering algorithm which, requires only the choice of similarity between pixels. The number of relevant clusters can then be estimated with the help of a hierarchical agglomerative clustering method. The clustering method is applied on data recorded in transmission configuration (cell side) as well as in reflection configuration (transducer side). Each cluster is unambiguously labeled thanks to conventional microscopy images carried on the very same cell. The acoustic properties of the inner structures of the cell such as the nucleus (with partial mitosis) and the cytoplasm are identified. The outskirt of the cell is composed of several clusters determined by the cell thickness as evidenced by correlating the clusters with AFM data. Data clustering on the transducer side reveals the existence of a very

thin layer (between 4.5 and 8.9 nm) not visible in transmission configuration, which may act as the adhesion layer for the cell. This thin layer has polymerlike acoustic properties. The adhesive area is imaged as evidenced by the acoustic energy loss after reflection at the transducer-cell interface. The clustering method is applied to seven other motoneurons fixed on the same sample. It is noteworthy that the results discussed here are consistent in any points with the clustering results on the seven other motoneurons: Brillouin frequencies, the correlation between the signal shape and the cell thickness, the detection of a thin adhesion layer, etc. The improvement of signal-to-noise ratio thanks to the clustering method is a strong step towards *in vitro* experiments. Indeed, while the investigated data takes hours to be acquired, living cell mechanical properties such as inner stiffness or adhesion to substrate may change significantly within 10 min. From this report, one can conclude that it is possible to resolve the nucleus position or the adhesion part of the cell with faster acquisition rate, at the expense of lower experimental signal-to-noise ratio.

ACKNOWLEDGMENTS

E.P. acknowledge very fruitful discussions about data clustering with Matt Clarke. E.P. would like to thank the support of INP (CNRS) and INSP scientific board, L.B. and A.H. acknowledge the support of Sorbonne University through the Emergence program.

[1] A. Shinde, K. Illath, P. Gupta, P. Shinde, K.-T. Lim, M. Nagai, and T. Santra, A review of single-cell adhesion force kinetics and applications, Cells **10**, 577 (2021).

[2] C. Peng, M. Chen, J. B. Spicer, and X. Jiang, Acoustics at the nanoscale (nanoacoustics): A comprehensive literature review. Part I: Materials, devices and selected applications, Sens. Actuators A: Phys. **332**, 112719 (2021).

[3] R. J. Smith, F. Pérez-Cota, L. Marques, and M. Clark, 3D phonon microscopy with sub-micron axial-resolution, Sci. Rep. **11**, 3301 (2021).

[4] C. Rossignol, N. Chigarev, and M. C. Durrieu, *In Vitro* picosecond ultrasonics in a single cell, Appl. Phys. Lett. **93**, 123901 (2008).

[5] S. Danworaphong, M. Tomoda, and O. B. Wright, Three-dimensional imaging of biological cells with picosecond ultrasonics, Appl. Phys. Lett. **106**, 163701 (2015).

[6] F. Perez-Cota, R. J. Smith, and M. Clark, New insights into the mechanical properties of *Acanthamoeba castellanii* cysts as revealed by phonon microscopy, Biomed. Opt. Express **10**, 2399 (2019).

[7] A. Viel, E. Péronne, and L. Belliard, Picosecond ultrasounds as elasticity probes in neuron-like cells models, Appl. Phys. Lett. **115**, 213701 (2019).

[8] L. Liu, A. Viel, and B. Audoin, Remote imaging of single cell 3D morphology with ultrafast coherent phonons and their resonance harmonics, Sci. Rep. **9**, 6409 (2019).

[9] F. Perez-Cota, R. J. Smith, and M. Clark, Thin-film optoacoustic transducers for subcellular brillouin oscillation imaging of individual biological cells, Appl. Opt. **54**, 8388 (2015).

[10] F. Perez-Cota, R. J. Smith, and M. Clark, High resolution 3D imaging of living cells with sub-optical wavelength phonons, Sci. Rep. **6**, 39326 (2016).

[11] T. Dehoux, M. A. Ghanem, and B. Audoin, Probing single-cell mechanics with picosecond ultrasonics, Ultrasonics **56**, 160 (2015).

[12] T. Dehoux, M. A. Ghanem, and B. Audoin, All-optical broadband ultrasonography of single cells, Sci. Rep. **5**, 8650 (2015).

[13] M. A. Ghanem, T. Dehoux, and B. Audoin, Opto-acoustic microscopy reveals adhesion mechanics of single cells, Rev. Sci. Instrum. **89**, 014901 (2018).

[14] L. Liu, L. Plawinski, and B. Audoin, Label-free multiparametric imaging of single cells: Dual picosecond optoacoustic microscopy, J. Biophotonics **12**, e201900045 (2019).

[15] A. Hamraoui, O. Sénépart, M. Schneider, S. Malaquin, E. Péronne, L. Becerra, F. Semprez, C. Legay, and L. Belliard, Correlative imaging of motoneuronal cell elasticity by pump and probe spectroscopy, Biophys. J. **120**, 1 (2021).

[16] H. Jia, S. Ding, X. Xu, and R. Nie, The latest research progress on spectral clustering, Neural Comput. Appl. **24**, 1477 (2014).

[17] Details of the chemicals (and their manufacturers) used during the sample preparation. Deionized water (Milli-*Q*). PBS or Phosphate buffered saline 1X (Gibco). Glutaraldehyde (Sigma-Aldrich). Rabbit polyclonal anti-bêta actin ab8227 (Abcam, Cambridge UK). Alexa Fluor 488 goat antirabbit 10729174 (Thermo Fisher Scientific). DAPI or 40, 6-diamidino-2-phenylindole (ThermoFisher Molecular Probes).

[18] M. Meila and J. Shi, in *Advances in Neural Information Processing Systems*, Vol. 13, edited by T. Leen, T. Dietterich, and V. Tresp (MIT Press, Cambridge, Massachusetts, 2001), p. 873.

[19] While the eigenvalues and eigenvectors are uniquely defined by the data, the *k*-means algorithm can lead to different clustering results since the results depend on the initial choice of the *k* centroid. Therefore, it is advised to run the *k*-means algorithm several times to look for the best results (i.e., minimum intracluster distances and maximum intercluster distances). We find a good stability of the results when *k*-means algorithm is run 400 times.

[20] A. Huynh, E. Péronne, C. Gingreau, X. Lafosse, A. Lemaître, B. Perrin, R. Vacher, B. Rufflé, and M. Foret, Temperature dependence of hypersound attenuation in silica films via picosecond acoustics, Phys. Rev. B **96**, 174206 (2018).

[21] T. Dehoux and B. Audoin, Non-invasive optoacoustic probing of the density and stiffness of single biological cells, J. Appl. Phys. **112**, 124702 (2012).